

TokenSplat: Token-aligned 3D Gaussian Splatting for Feed-forward Pose-free Reconstruction

Yihui Li^{1,2}, Chengxin Lv^{1,2}, Zichen Tang^{1,3}, Hongyu Yang^{3*}, Di Huang^{1,2}

¹ State Key Laboratory of Complex and Critical Software Environment, Beijing, China

² School of Computer Science and Engineering, Beihang University, China

³ School of Artificial Intelligence, Beihang University, China

{kidleyh, chengxinlv, zctang, hongyuyang, dhuang}@buaa.edu.cn

Abstract

We present **TokenSplat**, a feed-forward framework for joint 3D Gaussian reconstruction and camera pose estimation from unposed multi-view images. At its core, **TokenSplat** introduces a **Token-aligned Gaussian Prediction** module that aligns semantically corresponding information across views directly in the feature space. Guided by coarse token positions and fusion confidence, it aggregates multi-scale contextual features to enable long-range cross-view reasoning and reduce redundancy from overlapping Gaussians. To further enhance pose robustness and disentangle viewpoint cues from scene semantics, **TokenSplat** employs learnable camera tokens and an **Asymmetric Dual-Flow Decoder (ADF-Decoder)** that enforces directionally constrained communication between camera and image tokens. This maintains clean factorization within a feed-forward architecture, enabling coherent reconstruction and stable pose estimation without iterative refinement. Extensive experiments demonstrate that **TokenSplat** achieves higher reconstruction fidelity and novel-view synthesis quality in pose-free settings, and significantly improves pose estimation accuracy compared to prior pose-free methods. Project page: <https://kidleyh.github.io/tokensplat/>.

1. Introduction

3D Gaussian Splatting (3DGS) [19] has recently emerged as an efficient alternative to neural radiance fields (NeRFs) [26], enabling high-quality rendering with significantly faster performance. Despite this progress, most existing 3DGS-based reconstruction pipelines [5, 21, 23, 25, 39, 45] rely on per-scene optimization, which restricts their scalability and limits generalization across diverse scenes. Recent feed-forward variants [1, 4, 17, 40, 50] alleviate this by predicting 3D Gaussians directly from input images, but their applicability remains constrained by the requirement

for accurate camera poses. Pose estimation via structure-from-motion (SfM) [29] is computationally expensive and prone to failure in challenging environments, significantly impacting reconstruction stability.

To reduce dependence on external poses, several approaches [3, 12, 31] jointly optimize camera poses and reconstruction through alternating pipelines. While effective in alleviating strict pose requirements, these methods still struggle to maintain reconstruction fidelity when many or densely captured images are involved. More recent pose-free frameworks [14, 30, 35, 44] attempt to infer both camera poses and 3D structure directly from sparse unposed images. However, these approaches typically encode scene information and viewpoint cues within the same feature embeddings, leading to representation entanglement that camera parameters become difficult to disentangle from scene content, and errors in pose estimation propagate to 3D reconstruction.

Furthermore, most existing pose-free methods rely on pixel-aligned 3DGS heads that generate Gaussians at pixel-level granularity. As the number of views increases, this pixel-centric prediction induces redundant and overlapping Gaussians, causing geometric blurring, color inconsistency, and reduced scene fidelity. Although some works [15, 37] attempt multi-view 3DGS attribute fusion to suppress redundancy, their local aggregation scope limits their ability to form globally coherent structure, often resulting in fragmented or unstable reconstructions.

To address these challenges, we propose **TokenSplat**, a feed-forward 3D Gaussian splatting framework that reconstructs 3D scenes from an arbitrary number of unposed images while jointly estimating camera poses. At its core lies the **Token-aligned Gaussian Prediction** module, which aligns semantically corresponding information across viewpoints directly in the feature space. Guided by coarse token positions and fusion confidence, this module adaptively aggregates multi-scale contextual features across views, en-

abling long-range cross-view reasoning and reducing redundancy from overlapping Gaussians. The aggregated tokens are subsequently decoded by a 3D Gaussian prediction head, which maps each token to multiple Gaussians. This one-to-many mapping decouples Gaussian density from pixel resolution, yielding denser and more expressive splats while preserving both structural integrity and semantic coherence.

To jointly optimize 3D reconstruction and camera pose estimation within a feed-forward architecture, we introduce learnable camera tokens and an *Asymmetric Dual-Flow Decoder (ADF-Decoder)* that regulates the interaction between pose reasoning and scene reconstruction. Without iterative refinement loops traditionally used to disentangle pose and geometry, maintaining clean factorization between camera parameters and scene features becomes crucial. Unlike symmetric attention mechanisms that allow bidirectional mixing and risk entangling viewpoint-specific cues with scene semantics, the ADF-Decoder imposes directionally constrained information flow between camera tokens and image tokens. Camera tokens extract robust geometric cues from image tokens to support accurate pose prediction, while only stabilized low-frequency pose alignment signals are propagated back to image tokens. Through disentangled yet mutually supportive representations, TokenSplat achieves stronger cross-view alignment, more stable pose estimation, and higher-fidelity reconstruction.

In summary, our main contributions are as follows:

- We propose *TokenSplat*, a feed-forward pose-free reconstruction framework that jointly estimates camera poses and 3D Gaussian scenes from unposed multi-view images, exhibiting strong generalization.
- We introduce *Token-aligned Gaussian Prediction* module that enables relatively long-range multi-view feature aggregation and high-quality Gaussian generation with reduced redundancy and fragmentation.
- We design an *Asymmetric Dual-Flow Decoder* that disentangles pose reasoning from scene encoding while enabling mutual reinforcement, leading to more accurate pose estimation and improved reconstruction fidelity.

2. Related Work

2.1. Feed-forward 3D Reconstruction

Neural radiance fields (NeRF) [26] and 3D Gaussian Splatting (3DGS) [19] have achieved impressive results in novel view synthesis. However, their scene-specific optimization restricts scalability and generalization across multiple scenes. To overcome this limitation, recent works [1, 2, 4, 32, 33, 41, 43, 47] have explored feed-forward approaches. These methods can reconstruct scenes without per-scene optimization and generalize to unseen environments. Some works [37, 42] further improve model effi-

ciency and capability by incorporating lightweight cost volume modules or introducing depth priors. However, most of these methods are still only applicable under sparse-view conditions, and their broader applicability remains limited due to the requirement for precise image poses as input.

2.2. Pose-Free 3D Scene Reconstruction

Feed-forward methods that rely on camera parameters [4, 36, 46] typically obtain them via structure-from-motion (SfM) tools such as COLMAP [29], a process that can be complex and error-prone. Some approaches jointly optimize camera poses and scene representations, but they often require inefficient pipelines. For instance, PF3Splat [11] relies on off-the-shelf feature descriptors (LightGlue [24]) and RANSAC-based [9] pose initialization, and SelfSplat uses cross-view U-Nets [28] to predict depth and pose separately. More recently, pose-free methods [13, 14, 35, 44] reconstruct scenes directly in a canonical space without explicit pose inputs, leveraging point or feature matching. While these methods improve robustness with sparse inputs, they still rely on primitive pixel-aligned 3D Gaussians, which limits multi-view reconstruction fidelity and pose estimation accuracy.

To reduce redundancy and improve reconstruction consistency, FreeSplat [37] maintains global Gaussians and continuously fuses new view-specific Gaussians, while AnySplat [15] follows the VGGT [34] paradigm and directly performs voxel fusion on the predicted Gaussians. However, their purely local fusion of 3DGS attributes in 3D space lacks broader contextual reasoning, often resulting in fragmented or inconsistent scenes. In contrast, our method performs multi-view feature aggregation at the token level, integrating semantically corresponding features across views based on coarse token positions and confidence scores. This alleviates redundancy in overlapping regions, and produces structurally coherent and complete reconstructions.

3. Method

3.1. Problem Formulation

We aim to learn a feed-forward network that jointly reconstructs 3D Gaussians and predicts camera poses from a sequence of N unposed images $\{\mathbf{I}_i\}_{i=1}^N$, where $\mathbf{I}_i \in \mathbb{R}^{H \times W \times 3}$. For 3D reconstruction, we predict a set of 3D Gaussians in a canonical 3D space:

$$\{(\mu_g, \sigma_g, r_g, s_g, c_g)\}_{g=1}^G, \quad (1)$$

where each Gaussian is parameterized by its center $\mu_g \in \mathbb{R}^3$, opacity $\sigma_g \in \mathbb{R}^+$, rotation quaternion $r_g \in \mathbb{R}^4$, scale $s_g \in \mathbb{R}^3$, and spherical harmonics (SH) coefficients $c_g \in \mathbb{R}^{3 \times (k+1)^2}$ of degree k , following [18]. For camera pose estimation, the network predicts per-view poses \mathbf{P}_i that trans-

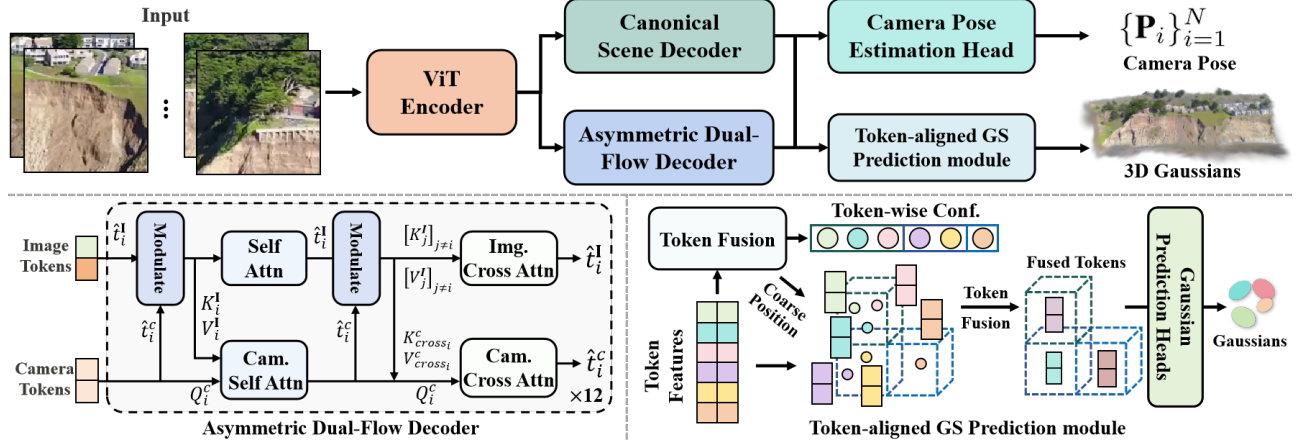


Figure 1. Overview of TokenSplat. TokenSplat performs feed-forward 3D Gaussian reconstruction and camera pose estimation from unposed images. A shared ViT encoder extracts image tokens, which are processed by the Canonical Scene Decoder and the Asymmetric Dual-Flow Decoder (ADF-Decoder). The fused tokens are then used by the Token-aligned Gaussian Prediction module and the camera pose head to generate dense 3D Gaussians and accurate poses.

form each input image \mathbf{I}_i into the canonical reference view \mathbf{I}_1 . Formally, the model learns a mapping:

$$f_{\theta} : \{\mathbf{I}_i\}_{i=1}^N \mapsto \{(\mu_g, \sigma_g, r_g, s_g, c_g)\}_{g=1}^G \cup \{\mathbf{P}_i\}_{i=1}^N. \quad (2)$$

During training, both the 3D Gaussian attributes and camera poses are jointly optimized.

3.2. Architecture

As illustrated in Fig. 1, our method is an Transformer-based architecture for feed-forward 3D reconstruction from unposed images. Each input view is first encoded into image tokens via a shared *ViT Encoder*. The reference view \mathbf{I}_1 is processed by a *Canonical Scene Decoder*, which uses cross-attention to integrate information from other views and establish a canonical scene representation. The remaining views are processed by the *Asymmetric Dual-Flow Decoder (ADF-Decoder)*, which refines both image and learnable camera tokens through directionally constrained communication, effectively disentangling camera parameters from image features. The outputs of these decoders are then utilized in two parallel branches: the *Camera Pose Estimation Head* predicts per-view camera transformations, while the *Token-aligned Gaussian Prediction module* aggregates multi-view tokens in the feature space and generates dense, coherent 3D Gaussians through its prediction head. This unified feed-forward design enables consistent multi-view reconstruction and robust pose estimation without any iterative refinement.

ViT Encoder. For each input view, the RGB image is divided into patches and embedded as a sequence of image tokens. Optionally, following [44], camera intrinsics are encoded as an additional token via a linear layer and concatenated with the image tokens along the spatial dimension to

mitigate scale ambiguity. Each view’s tokens are independently processed by a weight-shared ViT encoder, without cross-view interaction.

Canonical Scene Decoder. To establish a canonical scene representation, the reference view \mathbf{I}_1 is decoded using a ViT decoder with cross-attention to other views. This ensures that multi-view context is efficiently captured for the reference view and provides a consistent basis for reconstructing the 3D scene. The canonical representation facilitates the subsequent refinement of camera and scene features for the remaining views.

3.3. Asymmetric Dual-Flow Decoder

The ADF-Decoder is designed to jointly refine image and camera representations while explicitly disentangling scene content from camera parameters. To prevent entangling viewpoint-specific cues with scene semantics, it employs an *asymmetric update scheme* that image tokens primarily aggregate scene context, whereas camera tokens extract geometric cues from image tokens and propagate only stabilized pose signals back. This design enables accurate pose estimation and high-fidelity 3D reconstruction in a single feed-forward pass.

Token Initialization. Image tokens are generated by the shared ViT encoder. Camera tokens are initialized from learnable embeddings and duplicated for the $N - 1$ non-reference views to provide per-view pose representations. At each decoder layer, camera tokens interact with the corresponding image tokens through directionally constrained attention, allowing them to extract view-specific geometric cues while preventing unnecessary feature mixing.

Self-Attention. The ADF-Decoder consists of 12 decoder blocks. Within each block, self-attention is applied sepa-

rately to image and camera tokens. Image tokens integrate intra-view context to capture local scene structures and enhance reconstruction. Camera tokens attend to their corresponding image tokens to extract geometric cues for pose estimation. Formally, for view i , let \hat{t}_i^I denote the image tokens and \hat{t}_i^c denote the camera token. They are projected to queries, keys, and values Q_i^I (Q_i^c), K_i^I , and V_i^I . The updates are computed as:

$$\hat{t}_i^I \leftarrow \text{Softmax}\left(Q_i^I K_i^I{}^\top / \sqrt{d}\right) V_i^I, \quad (3)$$

$$\hat{t}_i^c \leftarrow \text{Softmax}\left(Q_i^c K_i^I{}^\top / \sqrt{d}\right) V_i^I, \quad (4)$$

where d is the corresponding dimensionality of the queries and keys. By updating camera tokens through their interaction with image tokens of the same view, the decoder extracts robust geometric features to support pose prediction. **Image Token Cross-View Attention.** To capture global multi-view context and enforce inter-view consistency, each view performs cross-attention over tokens from other views while explicitly avoiding interactions with its own tokens. This prevents information leakage across views and ensures complementary cues are integrated from the rest of the scene. For the image tokens of view I_i , the keys and values from other views are concatenated along the spatial dimension:

$$[K_j^I]_{j \neq i} = K_1^I \parallel \dots \parallel K_{i-1}^I \parallel K_{i+1}^I \parallel \dots \parallel K_N^I, \quad (5)$$

$$[V_j^I]_{j \neq i} = V_1^I \parallel \dots \parallel V_{i-1}^I \parallel V_{i+1}^I \parallel \dots \parallel V_N^I. \quad (6)$$

The image tokens are then updated via cross-attention:

$$\hat{t}_i^I \leftarrow \text{Softmax}\left(Q_i^I [K_j^I]_{j \neq i}{}^\top / \sqrt{d}\right) [V_j^I]_{j \neq i}. \quad (7)$$

To reduce computation with many views, a hyperparameter pnv limits each view’s attention to its $pnv - 1$ neighbors, balancing context and efficiency.

Camera Token Cross-Attention. Updating camera tokens solely via other camera tokens or solely via image tokens is insufficient to capture global geometry. Therefore, each camera token interacts with both image and camera tokens from other views, allowing it to aggregate multi-view geometric cues for more accurate camera pose estimation.

For view I_i , let \hat{t}_i^c be its camera token. All camera tokens are projected to obtain K^c and V^c . Each \hat{t}_j^c for $j \neq i$ is replicated to match the number of image tokens of other views, and then summed with the image token keys and values to form the cross-attention inputs:

$$K_{cross_i}^c = [K_j^I]_{j \neq i} + [\text{repeat}(K_j^c)]_{j \neq i}, \quad (8)$$

$$V_{cross_i}^c = [V_j^I]_{j \neq i} + [\text{repeat}(V_j^c)]_{j \neq i}. \quad (9)$$

The camera token is updated as:

$$\hat{t}_i^c \leftarrow \text{Softmax}\left(Q_i^c K_{cross_i}^c{}^\top / \sqrt{d}\right) V_{cross_i}^c. \quad (10)$$

Pre- and Post-Modulation. Due to differences in token counts and information content between image and camera tokens, image tokens are modulated with corresponding camera tokens both before and after attention. This stabilizes updates, reinforces disentanglement between pose and scene features, and ensures that pose cues guide reconstruction without contaminating scene semantics.

3.4. Token Fusion for Scene Reconstruction

The **Token-aligned Gaussian Prediction** module aggregates multi-view features and predicts dense 3D Gaussians for scene reconstruction. It comprises a **Token Fusion** operation and a **Gaussian Prediction Head**. Unlike traditional pixel-aligned Gaussian methods, which directly predict dense Gaussians for each pixel and suffer from redundancy and geometric blurring in dense multi-view setups, our method fuses features across tokens to produce more consistent and efficient 3D Gaussians.

Token Fusion. The token fusion operation first predicts coarse positions and fusion confidence for each token. Tokens are then grouped based on spatial proximity with a spatial grouping size ϵ , and fused using softmax-normalized confidence scores. This produces a set of merged tokens with consolidated features and coarse positions. The fusion network adopts a DPT-based architecture [27], similar to [44], with the number of predicted parameters adjusted.

Gaussian Prediction Head. For each fused token, the Gaussian prediction heads generate denser Gaussians, including positional offsets relative to the token and Gaussian attributes. Multi-scale features $\{F_i\}_{i=1}^{n_l}$ from different layers of the Transformer decoder corresponding to the fused tokens are first upsampled and linearly projected:

$$\hat{F}_i = Proj_i(F_i), \quad i = 1, \dots, n_l. \quad (11)$$

Channel dimensions are unified, and the features are upsampled according to layer scale (larger upsampling for lower layers, smaller for higher layers). Features are then progressively fused from deep to shallow layers using the residual fusion module RF composed of residual blocks and upsampling:

$$F_{n_l}^{fusion} = RF_{n_l}(\hat{F}_{n_l}), \quad (12)$$

$$F_i^{fusion} = RF_i(\hat{F}_i, F_{i+1}^{fusion}). \quad (13)$$

Residual blocks enhance feature expressiveness, while upsampling spatially aligns semantic and detailed information. The resulting fused features combine fine-grained details with rich semantic context.

Finally, the fused high-resolution features are passed through a prediction block consisting of upsampling and linear layers, producing continuous tensors representing the final Gaussian predictions. For full architectural details of the token-aligned Gaussian prediction heads, please refer to the appendix.

3.5. Camera Pose Estimation Head

The camera pose estimation head predicts the extrinsic parameters for each input view (excluding the reference view \mathbf{I}_1). It takes the per-view camera tokens produced by the decoder as input and applies a linear projection to regress the camera transformation \mathbf{P} for each view. Jointly optimizing camera poses alongside the token-aligned Gaussian reconstruction encourages the network to learn geometrically consistent 3D features, which improves both pose estimation and scene reconstruction accuracy.

3.6. Loss Functions

Image Rendering Loss. We supervise the model using the ground-truth target RGB images. The rendering loss combines an L2 loss and a perceptual LPIPS loss [48]:

$$\mathcal{L}_{render} = \mathcal{L}_2(\mathbf{I}, \hat{\mathbf{I}}) + \lambda_{lrips} \mathcal{L}_{lrips}(\mathbf{I}, \hat{\mathbf{I}}), \quad (14)$$

where \mathbf{I} and $\hat{\mathbf{I}}$ denote the ground-truth and rendered images, and λ_{lrips} balances the perceptual term.

Camera Pose Loss. The camera pose head predicts each view’s extrinsic parameters relative to the reference view \mathbf{I}_1 . We supervise the predictions with a combination of MSE and Unit Dual Quaternion (DQ) alignment loss [6, 8, 16], which jointly represents rotation and translation to avoid inconsistencies from separate predictions. The alignment loss is defined as:

$$\mathcal{L}_{align} = \|p^I - p\hat{p}^*\| + \|p^I - \hat{p}p^*\|, \quad (15)$$

where p and \hat{p} are the predicted and ground-truth unit DQs, and p^* denotes the conjugate. The overall camera pose loss is:

$$\mathcal{L}_{pose} = \mathcal{L}_{MSE}(\mathbf{P}, \hat{\mathbf{P}}) + \mathcal{L}_{align}. \quad (16)$$

Total Loss. The model is trained end-to-end with the total loss:

$$\mathcal{L} = \mathcal{L}_{render} + \lambda_c \mathcal{L}_{pose}, \quad (17)$$

where λ_c balances the contribution of the camera pose supervision.

4. Experiment

We evaluate our method on novel view synthesis (NVS) and camera pose estimation across sparse and long-sequence real-world datasets.

4.1. Experimental Settings

Datasets. We conduct experiments on ScanNet [7] and RealEstate10K (RE10K) [49]. For ScanNet, we adopt the training/testing splits from [37], and for RE10K we follow [44]. Both settings ensure a direct and consistent comparison with prior work.

Baselines and Metrics. We evaluate NVS performance using PSNR, SSIM [38], and LPIPS [48]. For camera pose estimation, we report Absolute Translation Error (ATE), Relative Translation Error (RPE-t), and Relative Rotation Error (RPE-r). We compare against generalizable NVS methods, including (1) Pose-required: MVSplat [4] and FreeSplat [37]; and (2) Pose-free: NoPoSplat [44], VicaSpalt [22], SPFSplat [13], and AnySplat [15]. Pose estimation comparisons are conducted only with pose-free methods.

Implementation Details. Our method is implemented in PyTorch. The encoder follows [44] and adopts a ViT-Large backbone with a patch size of 16. We initialize the encoder-decoder and Gaussian center head with MAST3R [20] weights, while the ADF-Decoder and remaining heads are randomly initialized.

Following [22], we train and evaluate on RE10K under both 4-view and 8-view reference settings, and further perform cross-dataset generalization tests on ScanNet. For ScanNet, we adopt the 3-view and 10-view settings from [37], where the 10-view configuration is obtained by augmenting the 3-view setup with additional reference views. To stress-test multi-view scalability on longer sequences, we also design a 28-view evaluation on ScanNet.

For fair comparisons, we follow [4, 13, 22] and report all quantitative results at a fixed resolution of 256×256 . Additional details are provided in the appendix.

4.2. Experimental Results

Performance on Multi-view NVS. The results are shown on the left side of Tab. 1 and Tab. 2. Here, AnySplat refers to zero-shot results trained on other datasets, while AnySplat* denotes the results we achieved after fine-tuning on the corresponding dataset. As can be seen, TokenSplat consistently outperforms state-of-the-art pose-free methods, including those specifically designed for multi-view input such as VicaSplat and AnySplat, which leverage cross-neighbor attention and pixel-aligned Gaussian fusion, respectively. In dense-view scenarios, TokenSplat even surpasses pose-dependent methods like FreeSplat, achieving 0.95 dB higher PSNR on RE10K with 8 views.

For the 28-view evaluation, we use models trained with 10 views. Despite the difference in view counts, TokenSplat maintains stable reconstruction quality, while competing methods, including AnySplat, which fuses pixel-aligned Gaussians by predicting fusion confidence, and FreeSplat, show degradation. We attribute this to the Gaussian-level fusion strategy used in these methods, which accumulates inconsistencies and redundancies as more views are incorporated. In contrast, TokenSplat performs fusion in feature space, enhancing cross-view reasoning and reducing redundancy in long-sequence, high-density scenarios. Moreover, as the number of input images increases, our model achieves a higher SSIM of 0.061 over FreeSplat, while also show-

Table 1. Quantitative results of NVS on RE10K with varying reference views (left) and cross-dataset generalization to ScanNet (right). The **best** and second-best values are highlighted.

Method		RE10K (4 views)			RE10K (8 views)			ScanNet (4 views)			ScanNet (8 views)		
		PSNR \uparrow	SSIM \uparrow	LPIPS \downarrow	PSNR \uparrow	SSIM \uparrow	LPIPS \downarrow	PSNR \uparrow	SSIM \uparrow	LPIPS \downarrow	PSNR \uparrow	SSIM \uparrow	LPIPS \downarrow
Pose-required	MVSplat	23.82	0.792	0.201	23.96	0.802	0.164	24.48	0.854	0.225	23.11	0.761	0.296
	FreeSplat	<u>24.99</u>	0.814	<u>0.162</u>	<u>25.20</u>	<u>0.829</u>	0.179	<u>27.23</u>	<u>0.873</u>	0.196	<u>24.64</u>	<u>0.819</u>	<u>0.241</u>
Pose-free	NoPoSplat	24.87	0.813	0.169	25.01	0.832	<u>0.163</u>	27.10	0.864	0.189	24.26	0.796	0.269
	VicaSplat	24.65	0.795	0.206	24.50	0.806	0.164	26.46	0.837	0.214	22.95	0.765	0.306
	SPFSplat	24.98	0.819	0.166	25.18	0.828	0.169	27.17	0.873	<u>0.185</u>	24.15	0.793	0.263
	Anysplat*	20.28	<u>0.657</u>	0.251	20.93	0.746	0.284	22.74	0.768	<u>0.242</u>	21.83	0.673	0.358
	Anysplat	15.55	0.475	0.424	16.23	0.520	0.401	17.07	0.580	0.436	16.72	0.577	0.457
	Ours	25.14	0.834	0.156	26.15	0.858	0.135	28.15	0.884	0.178	25.15	0.824	0.233

Table 2. Quantitative results of NVS on ScanNet under varying numbers of views. The **best** and second-best values are highlighted.

Method		3 views			10 views			28 views		
		PSNR \uparrow	SSIM \uparrow	LPIPS \downarrow	PSNR \uparrow	SSIM \uparrow	LPIPS \downarrow	PSNR \uparrow	SSIM \uparrow	LPIPS \downarrow
Pose-required	MVSplat	24.98	0.784	0.228	23.12	0.768	0.236	22.26	0.714	0.336
	FreeSplat	25.63	<u>0.804</u>	0.218	<u>25.38</u>	<u>0.815</u>	<u>0.189</u>	<u>24.30</u>	<u>0.798</u>	<u>0.249</u>
Pose-free	NoPoSplat	25.55	0.803	<u>0.213</u>	24.21	0.811	0.198	23.21	0.764	0.268
	VicaSplat	24.54	0.786	<u>0.226</u>	23.73	0.760	0.268	22.37	0.709	0.316
	SPFSplat	25.85	0.788	0.229	24.63	0.773	0.226	23.54	0.775	0.261
	Anysplat*	19.84	0.658	0.314	22.06	0.687	0.353	21.17	0.680	0.357
	Anysplat	15.05	0.415	0.416	16.73	0.522	0.437	16.58	0.561	0.439
	Ours	26.57	0.841	0.189	26.83	0.851	0.179	26.87	0.859	0.173

ing improved novel view synthesis quality. These results demonstrate the scalability of our approach to a larger number of views.

In Fig. 2, our method consistently produces clearer and more realistic novel view renderings in challenging cases. Ours better preserves fine structural details and reduces artifacts and blurring. See more visualizations in appendix.

Pose Estimation. The results are shown in the left side of Tab. 3 and Tab. 4. For NoPoSplat, poses are estimated via PnP [10] with RANSAC [9] from predicted Gaussian centers, while other methods directly output camera poses. TokenSplat consistently surpasses pose-free baselines on RE10K, reducing RPE-R (lower is better) by 0.335 and 0.147 compared to VicaSplat and AnySplat under the 8-view setting. This gain stems from our directionally constrained ADF-Decoder, which enforces disentangled interaction between camera and image tokens, leading to more stable pose learning. On ScanNet, the model maintains accurate pose estimation under the 28-view setting, reducing ATE by 0.018 over AnySplat, confirming both robustness and scalability of TokenSplat in multi-view scenarios.

Cross-Dataset Generalization. To assess zero-shot generalization, we train TokenSplat on RE10K and directly evaluate it on ScanNet. As shown in the right halves of both Tab. 1 and Tab. 3, which report cross-dataset results, our method surpasses all SOTA approaches on both novel view synthesis and pose estimation. Compared to FreeSplat, To-

kenSplat achieves up to 0.92/0.51 dB higher PSNR, and reduces ATE by 0.013/0.033 over SPFSplat. In Fig. 3, TokenSplat preserves coherent geometry and clearly reconstructed scene structures. Notably, fine details such as furniture boundaries are better preserved than in competing methods, demonstrating the effectiveness of our method across unseen scenes. The camera pose head further ensures reliable pose estimation under novel camera configurations, jointly contributing to superior cross-dataset performance.

Scene-level Visualization. To further illustrate the reconstruction quality, Fig. 4 presents scene-level visualizations, where the camera is pulled back to reveal the global 3D Gaussian structures, along with several rendered novel views. AnySplat, which directly fuses 3D Gaussians, exhibits noticeable misalignment artifacts and visible fusion cracks across viewpoints. FreeSplat generates numerous scattered Gaussians, while NoPoSplat and SPFSplat show poor scalability and fail to generalize to unseen distant viewpoints. In contrast, our method preserves coherent and geometrically consistent reconstructions, even when rendered from viewpoints far beyond the training range.

4.3. Ablation Analysis

We perform ablation studies on RE10K (8 views), summarized in Tab. 5. Compared to our full model (a), (b) replacing the Token-aligned Gaussian Prediction with a pixel-aligned Gaussian head degrades both reconstruction and

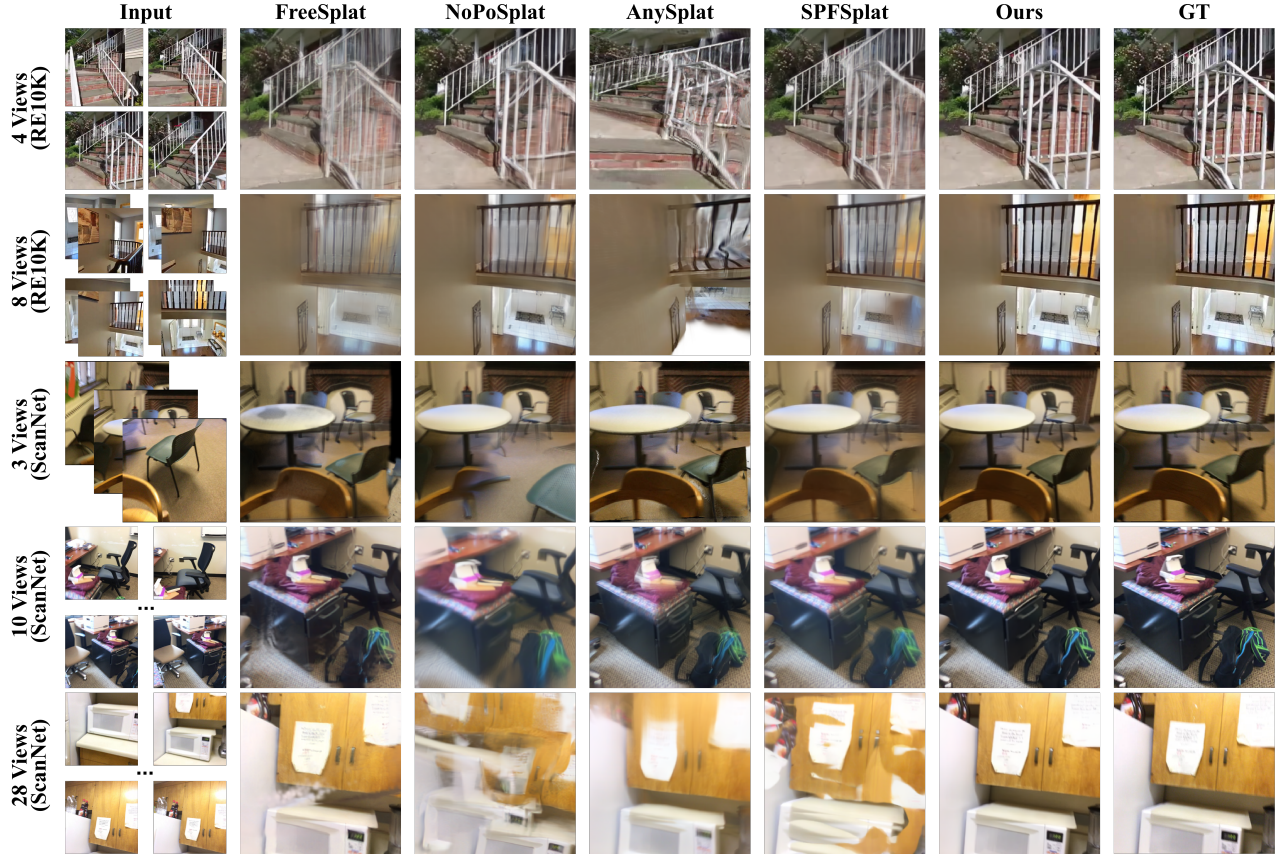


Figure 2. Qualitative comparison on RE10K and ScanNet under varying numbers of reference views.

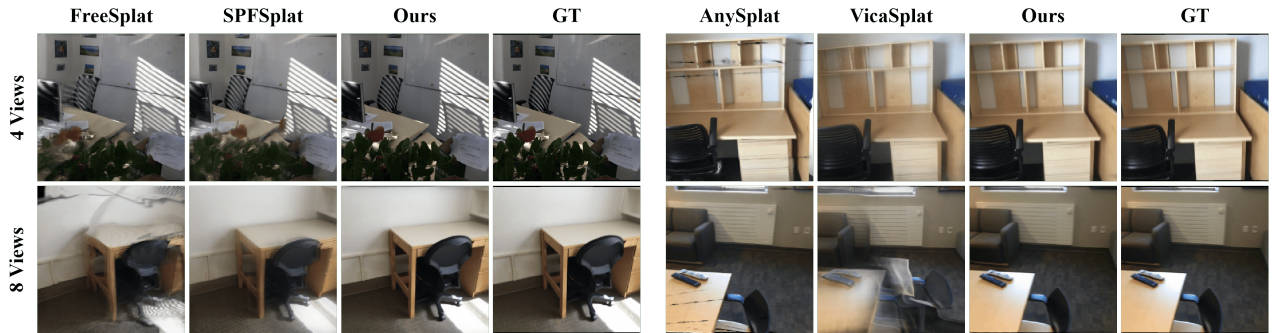


Figure 3. Cross-dataset generalization from RE10K to ScanNet.

Table 3. Quantitative results of pose prediction on RE10K with diverse views (left) and cross-dataset generalization to ScanNet (right).

Method	RE10K (4 views)			RE10K (8 views)			ScanNet (4 views)			ScanNet (8 views)		
	ATE↓	RPE-t↓	RPE-r↓	ATE↓	RPE-t↓	RPE-r↓	ATE↓	RPE-t↓	RPE-r↓	ATE↓	RPE-t↓	RPE-r↓
NoPoSplat	0.032	0.070	1.923	0.123	0.135	1.757	0.139	0.259	2.135	0.208	0.268	4.098
VicaSplat	<u>0.027</u>	0.057	<u>1.392</u>	0.021	0.031	0.793	0.095	0.234	2.735	0.163	0.197	3.162
SPFSplat	0.036	0.078	3.113	0.037	0.047	2.117	<u>0.075</u>	0.201	2.658	0.121	0.173	3.676
Anysplat*	0.028	<u>0.051</u>	1.515	<u>0.020</u>	<u>0.025</u>	<u>0.578</u>	<u>0.092</u>	0.238	<u>1.902</u>	<u>0.098</u>	<u>0.150</u>	<u>2.016</u>
Anysplat	0.033	0.055	1.624	0.024	0.029	0.605	0.099	0.268	1.995	0.101	0.157	2.114
Ours	0.016	0.034	1.054	0.012	0.019	0.458	0.062	0.159	1.162	0.088	0.130	1.672

Table 4. Quantitative results of pose prediction on ScanNet with diverse views. The **best** and second-best values are highlighted.

Method	3 views			10 views			28 views		
	ATE↓	RPE-t↓	RPE-r↓	ATE↓	RPE-t↓	RPE-r↓	ATE↓	RPE-t↓	RPE-r↓
NoPoSplat	0.055	0.218	2.041	0.167	0.175	5.537	0.187	0.197	4.551
VicaSplat	0.075	0.268	1.803	0.171	0.231	3.768	0.243	0.189	3.725
SPFSplat	0.104	0.336	2.351	0.155	0.167	3.249	0.207	0.216	4.428
Anysplat*	0.057	0.198	1.567	0.135	0.181	1.165	0.097	0.094	1.239
Anysplat	0.062	0.213	1.611	0.148	0.196	1.192	0.098	0.091	1.362
Ours	0.041	0.147	1.252	0.093	0.135	0.799	0.080	0.075	0.709

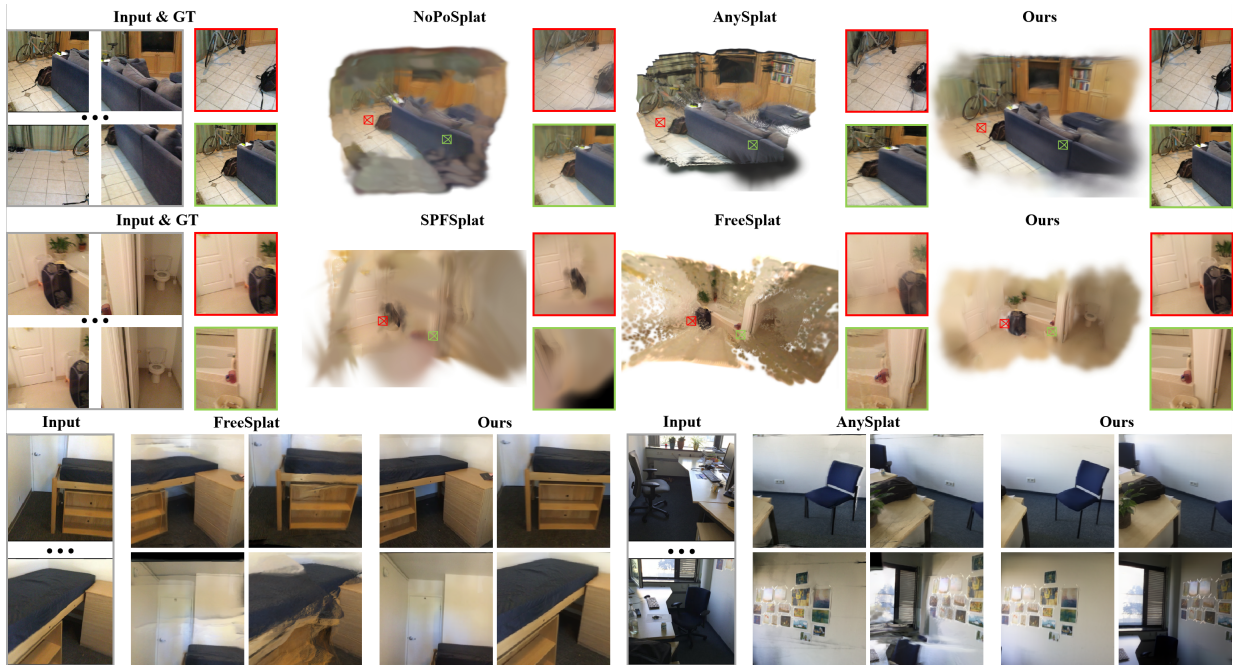


Figure 4. Scene-level visualizations and multiple novel viewpoints renderings.

Table 5. Component ablations on RE10K (8 view).

Method	PSNR↑	SSIM↑	LPIPS↓	ATE↓	RPE-t↓	RPE-r↓
(a) Ours	26.15	0.858	0.135	0.012	0.019	0.458
(b) w Pixel Head	25.33	0.832	0.159	0.018	0.028	0.496
(c) w Any. Fusion.	25.77	0.847	0.148	0.020	0.027	0.489
(d) w/o ADF-Dec.	25.88	0.845	0.146	0.023	0.029	0.504
(e) w/o intrin. emb.	25.54	0.835	0.157	0.016	0.022	0.471

pose estimation, with SSIM dropping by 0.026 and RPE-r increasing by 0.038; (c) using AnySplat-style Gaussian fusion, which fuses pixel-aligned Gaussians by predicting per-Gaussian fusion confidence, improves over the pixel-aligned head but still underperforms our token-based fusion, with PSNR 0.38 dB lower; (d) replacing the ADF-decoder with a standard ViT decoder that concatenates camera and image tokens for attention increases pose entanglement, leading to 0.046 higher RPE-r and 0.011 higher LPIPS (lower is better), highlighting the benefit of direc-

tionally constrained communication for disentangling pose and image features; (e) removing the known intrinsic camera embedding reduces reconstruction quality, as the model struggles to capture scale, though pose estimation remains competitive. Overall, these results demonstrate the effectiveness of our model designs for accurate multi-view reconstruction and camera pose estimation.

5. Conclusion

We present *TokenSplat*, a feed-forward framework for joint 3D reconstruction and camera pose estimation from unposed multi-view images. By leveraging token-based multi-view fusion and ADF-Decoder, it achieves clean feature disentanglement and stable aggregation, enabling coherent reconstruction without iterative refinement. *TokenSplat* consistently improves reconstruction and pose accuracy and generalizes well, achieving competitive zero-shot performance when trained on a single RE10K-scale dataset.

References

- [1] David Charatan, Sizhe Lester Li, Andrea Tagliasacchi, and Vincent Sitzmann. pixelsplat: 3d gaussian splats from image pairs for scalable generalizable 3d reconstruction. In *Proceedings of the IEEE/CVF conference on computer vision and pattern recognition*, pages 19457–19467, 2024. 1, 2
- [2] Anpei Chen, Zexiang Xu, Fuqiang Zhao, Xiaoshuai Zhang, Fanbo Xiang, Jingyi Yu, and Hao Su. Mvsnerf: Fast generalizable radiance field reconstruction from multi-view stereo. In *Proceedings of the IEEE/CVF international conference on computer vision*, pages 14124–14133, 2021. 2
- [3] Yu Chen and Gim Hee Lee. Dbarf: Deep bundle-adjusting generalizable neural radiance fields. In *Proceedings of the IEEE/CVF Conference on Computer Vision and Pattern Recognition*, pages 24–34, 2023. 1
- [4] Yuedong Chen, Haofei Xu, Chuanxia Zheng, Bohan Zhuang, Marc Pollefeys, Andreas Geiger, Tat-Jen Cham, and Jianfei Cai. Mvsplat: Efficient 3d gaussian splatting from sparse multi-view images. In *European Conference on Computer Vision*, pages 370–386. Springer, 2024. 1, 2, 5
- [5] Shin-Fang Chng, Sameera Ramasinghe, Jamie Sherrah, and Simon Lucey. Gaussian activated neural radiance fields for high fidelity reconstruction and pose estimation. In *European Conference on Computer Vision*, pages 264–280. Springer, 2022. 1
- [6] Clifford. Preliminary sketch of biquaternions. *Proceedings of the London Mathematical Society*, 1(1):381–395, 1871. 5
- [7] Angela Dai, Angel X Chang, Manolis Savva, Maciej Halber, Thomas Funkhouser, and Matthias Nießner. Scannet: Richly-annotated 3d reconstructions of indoor scenes. In *Proceedings of the IEEE conference on computer vision and pattern recognition*, pages 5828–5839, 2017. 5
- [8] Konstantinos Daniilidis. Hand-eye calibration using dual quaternions. *The International Journal of Robotics Research*, 18(3):286–298, 1999. 5
- [9] Martin A Fischler and Robert C Bolles. Random sample consensus: a paradigm for model fitting with applications to image analysis and automated cartography. *Communications of the ACM*, 24(6):381–395, 1981. 2, 6
- [10] Richard Hartley and Andrew Zisserman. *Multiple view geometry in computer vision*. Cambridge university press, 2003. 6
- [11] Sunghwan Hong, Jaewoo Jung, Heeseong Shin, Jisang Han, Jiaolong Yang, Chong Luo, and Seungryong Kim. Pf3plat: Pose-free feed-forward 3d gaussian splatting. *arXiv preprint arXiv:2410.22128*, 2024. 2
- [12] Sunghwan Hong, Jaewoo Jung, Heeseong Shin, Jiaolong Yang, Seungryong Kim, and Chong Luo. Unifying correspondence pose and nerf for generalized pose-free novel view synthesis. In *Proceedings of the IEEE/CVF Conference on Computer Vision and Pattern Recognition*, pages 20196–20206, 2024. 1
- [13] Ranran Huang and Krystian Mikolajczyk. No pose at all: Self-supervised pose-free 3d gaussian splatting from sparse views. *arXiv preprint arXiv:2508.01171*, 2025. 2, 5
- [14] Hanwen Jiang, Zhenyu Jiang, Yue Zhao, and Qixing Huang. Leap: Liberate sparse-view 3d modeling from camera poses. *arXiv preprint arXiv:2310.01410*, 2023. 1, 2
- [15] Lihan Jiang, Yucheng Mao, Linning Xu, Tao Lu, Kerui Ren, Yichen Jin, Xudong Xu, Mulin Yu, Jiangmiao Pang, Feng Zhao, et al. Anysplat: Feed-forward 3d gaussian splatting from unconstrained views. *arXiv preprint arXiv:2505.23716*, 2025. 1, 2, 5
- [16] Ladislav Kavan, Steven Collins, Carol O’Sullivan, and Jiri Zara. Dual quaternions for rigid transformation blending. *Trinity College Dublin*, 5:4, 2006. 5
- [17] Nikhil Keetha, Norman Müller, Johannes Schönberger, Lorenzo Porzi, Yuchen Zhang, Tobias Fischer, Arno Knapitsch, Duncan Zauss, Ethan Weber, Nelson Antunes, et al. Mapanything: Universal feed-forward metric 3d reconstruction. *arXiv preprint arXiv:2509.13414*, 2025. 1
- [18] Bernhard Kerbl, Georgios Kopanas, Thomas Leimkühler, and George Drettakis. 3d gaussian splatting for real-time radiance field rendering. *ACM Trans. Graph.*, 42(4):139–1, 2023. 2
- [19] Bernhard Kerbl, Georgios Kopanas, Thomas Leimkühler, and George Drettakis. 3d gaussian splatting for real-time radiance field rendering. *ACM Transactions on Graphics*, 42(4), 2023. 1, 2
- [20] Vincent Leroy, Johann Cabon, and Jérôme Revaud. Grounding image matching in 3d with mast3r. In *European Conference on Computer Vision*, pages 71–91. Springer, 2024. 5
- [21] Yihui Li, Chengxin Lv, Hongyu Yang, and Di Huang. Micro-macro wavelet-based gaussian splatting for 3d reconstruction from unconstrained images. In *Proceedings of the AAAI Conference on Artificial Intelligence*, pages 5057–5065, 2025. 1
- [22] Zhiqi Li, Chengrui Dong, Yiming Chen, Zhangchi Huang, and Peidong Liu. Vicasplat: A single run is all you need for 3d gaussian splatting and camera estimation from unposed video frames. *arXiv preprint arXiv:2503.10286*, 2025. 5, 1
- [23] Chen-Hsuan Lin, Wei-Chiu Ma, Antonio Torralba, and Simon Lucey. Barf: Bundle-adjusting neural radiance fields. In *Proceedings of the IEEE/CVF international conference on computer vision*, pages 5741–5751, 2021. 1
- [24] Philipp Lindenberger, Paul-Edouard Sarlin, and Marc Pollefeys. Lightglue: Local feature matching at light speed. In *Proceedings of the IEEE/CVF international conference on computer vision*, pages 17627–17638, 2023. 2
- [25] Tao Lu, Mulin Yu, Linning Xu, Yuanbo Xiangli, Limin Wang, Dahua Lin, and Bo Dai. Scaffold-gs: Structured 3d gaussians for view-adaptive rendering. In *Proceedings of the IEEE/CVF Conference on Computer Vision and Pattern Recognition*, pages 20654–20664, 2024. 1
- [26] Ben Mildenhall, Pratul P Srinivasan, Matthew Tancik, Jonathan T Barron, Ravi Ramamoorthi, and Ren Ng. Nerf: Representing scenes as neural radiance fields for view synthesis. *Communications of the ACM*, 65(1):99–106, 2021. 1, 2
- [27] René Ranftl, Alexey Bochkovskiy, and Vladlen Koltun. Vision transformers for dense prediction. In *Proceedings of the IEEE/CVF international conference on computer vision*, pages 12179–12188, 2021. 4

- [28] Olaf Ronneberger, Philipp Fischer, and Thomas Brox. U-net: Convolutional networks for biomedical image segmentation. In *International Conference on Medical image computing and computer-assisted intervention*, pages 234–241. Springer, 2015. 2
- [29] Johannes L Schonberger and Jan-Michael Frahm. Structure-from-motion revisited. In *Proceedings of the IEEE conference on computer vision and pattern recognition*, pages 4104–4113, 2016. 1, 2
- [30] Brandon Smart, Chuanxia Zheng, Iro Laina, and Victor Adrian Prisacariu. Splat3r: Zero-shot gaussian splatting from uncalibrated image pairs. *arXiv preprint arXiv:2408.13912*, 2024. 1
- [31] Cameron Smith, Yilun Du, Ayush Tewari, and Vincent Sitzmann. Flowcam: Training generalizable 3d radiance fields without camera poses via pixel-aligned scene flow. *arXiv preprint arXiv:2306.00180*, 2023. 1
- [32] Jiaxiang Tang, Zhaoxi Chen, Xiaokang Chen, Tengfei Wang, Gang Zeng, and Ziwei Liu. Lgm: Large multi-view gaussian model for high-resolution 3d content creation. In *European Conference on Computer Vision*, pages 1–18. Springer, 2024. 2
- [33] Shengji Tang, Weicai Ye, Peng Ye, Weihao Lin, Yang Zhou, Tao Chen, and Wanli Ouyang. Hisplat: Hierarchical 3d gaussian splatting for generalizable sparse-view reconstruction. *arXiv preprint arXiv:2410.06245*, 2024. 2
- [34] Jianyuan Wang, Minghao Chen, Nikita Karaev, Andrea Vedaldi, Christian Rupprecht, and David Novotny. Vggt: Visual geometry grounded transformer. In *Proceedings of the Computer Vision and Pattern Recognition Conference*, pages 5294–5306, 2025. 2
- [35] Peng Wang, Hao Tan, Sai Bi, Yinghao Xu, Fujun Luan, Kalyan Sunkavalli, Wenping Wang, Zexiang Xu, and Kai Zhang. Pf-lrm: Pose-free large reconstruction model for joint pose and shape prediction. *arXiv preprint arXiv:2311.12024*, 2023. 1, 2
- [36] Weijie Wang, Yeqing Chen, Zeyu Zhang, Hengyu Liu, Haoxiao Wang, Zhiyuan Feng, Wenkang Qin, Zheng Zhu, Donny Y Chen, and Bohan Zhuang. Volsplat: Rethinking feed-forward 3d gaussian splatting with voxel-aligned prediction. *arXiv preprint arXiv:2509.19297*, 2025. 2
- [37] Yunsong Wang, Tianxin Huang, Hanlin Chen, and Gim Hee Lee. Freesplat: Generalizable 3d gaussian splatting towards free view synthesis of indoor scenes. *Advances in Neural Information Processing Systems*, 37:107326–107349, 2024. 1, 2, 5
- [38] Zhou Wang, Alan C Bovik, Hamid R Sheikh, and Eero P Simoncelli. Image quality assessment: from error visibility to structural similarity. *IEEE transactions on image processing*, 13(4):600–612, 2004. 5
- [39] Zirui Wang, Shangzhe Wu, Weidi Xie, Min Chen, and Victor Adrian Prisacariu. Nerf-: Neural radiance fields without known camera parameters. 2021. 1
- [40] Christopher Wewer, Kevin Raj, Eddy Ilg, Bernt Schiele, and Jan Eric Lenssen. latentsplat: Autoencoding variational gaussians for fast generalizable 3d reconstruction. In *European conference on computer vision*, pages 456–473. Springer, 2024. 1
- [41] Haofei Xu, Anpei Chen, Yuedong Chen, Christos Sakaridis, Yulun Zhang, Marc Pollefeys, Andreas Geiger, and Fisher Yu. Murf: multi-baseline radiance fields. In *Proceedings of the IEEE/CVF Conference on Computer Vision and Pattern Recognition*, pages 20041–20050, 2024. 2
- [42] Haofei Xu, Songyou Peng, Fangjinhua Wang, Hermann Blum, Daniel Barath, Andreas Geiger, and Marc Pollefeys. Depthsplat: Connecting gaussian splatting and depth. In *Proceedings of the Computer Vision and Pattern Recognition Conference*, pages 16453–16463, 2025. 2
- [43] Yinghao Xu, Zifan Shi, Wang Yifan, Hansheng Chen, Ceyuan Yang, Sida Peng, Yujun Shen, and Gordon Wetstein. Grm: Large gaussian reconstruction model for efficient 3d reconstruction and generation. In *European Conference on Computer Vision*, pages 1–20. Springer, 2024. 2
- [44] Botao Ye, Sifei Liu, Haofei Xu, Xueting Li, Marc Pollefeys, Ming-Hsuan Yang, and Songyou Peng. No pose, no problem: Surprisingly simple 3d gaussian splats from sparse unposed images. *arXiv preprint arXiv:2410.24207*, 2024. 1, 2, 3, 4, 5
- [45] Zehao Yu, Anpei Chen, Binbin Huang, Torsten Sattler, and Andreas Geiger. Mip-splatting: Alias-free 3d gaussian splatting. In *Proceedings of the IEEE/CVF conference on computer vision and pattern recognition*, pages 19447–19456, 2024. 1
- [46] Cheng Zhang, Haofei Xu, Qianyi Wu, Camilo Cruz Gambardella, Dinh Phung, and Jianfei Cai. Pansplat: 4k panorama synthesis with feed-forward gaussian splatting. In *Proceedings of the Computer Vision and Pattern Recognition Conference*, pages 11437–11447, 2025. 2
- [47] Kai Zhang, Sai Bi, Hao Tan, Yuanbo Xiangli, Nanxuan Zhao, Kalyan Sunkavalli, and Zexiang Xu. Gs-lrm: Large reconstruction model for 3d gaussian splatting. In *European Conference on Computer Vision*, pages 1–19. Springer, 2024. 2
- [48] Richard Zhang, Phillip Isola, Alexei A Efros, Eli Shechtman, and Oliver Wang. The unreasonable effectiveness of deep features as a perceptual metric. In *Proceedings of the IEEE conference on computer vision and pattern recognition*, pages 586–595, 2018. 5
- [49] Tinghui Zhou, Richard Tucker, John Flynn, Graham Fyffe, and Noah Snavely. Stereo magnification: learning view synthesis using multiplane images. *ACM Transactions on Graphics (TOG)*, 37(4):1–12, 2018. 5
- [50] Zi-Xin Zou, Zhipeng Yu, Yuan-Chen Guo, Yangguang Li, Ding Liang, Yan-Pei Cao, and Song-Hai Zhang. Triplane meets gaussian splatting: Fast and generalizable single-view 3d reconstruction with transformers. In *Proceedings of the IEEE/CVF conference on computer vision and pattern recognition*, pages 10324–10335, 2024. 1

TokenSplat: Token-aligned 3D Gaussian Splatting for Feed-forward Pose-free Reconstruction

Supplementary Material

A1. More Implementation Details of Experiment

More Training Details. Our model is implemented using PyTorch, and all models are trained on a single A800 GPU. Comparable results can also be achieved on a single A6000 or A100 GPU by adjusting to a smaller batch size and increasing the number of training iterations. Following strategies similar to those in [44] and [22], we train with a batch size of 16, a learning rate of 2×10^{-5} for the backbone, and a learning rate of 2×10^{-4} for the other components for 30,000 iterations under the 2-view settings. Subsequently, for multi-view scenarios, we fine-tune the model for 100,000 iterations with a backbone learning rate of 4×10^{-6} , a learning rate of 4×10^{-5} for the other components, and a batch size of 1. For the 28-view test on ScanNet, we use the model trained under the 10-view setting to evaluate the model’s ability to generalize to a larger number of views. All other models, except for AnySplat, adopt a similar setup.

More Details of MVsplat and FreeSplat Results. All settings follow those specified in the official FreeSplat repository. For the 28-view results of FreeSplat on ScanNet, we use the model trained with the “fvf” setting (with the maximum number of views during training still set to 10), as this configuration offers better scalability and leads to higher performance for FreeSplat.

More Details of NoPoSplat Results. We use the official 2-view checkpoint from the repository and further fine-tune NoPoSplat with the exact same settings as our method to ensure a fair comparison. Additionally, all methods use the same view alignment protocol as NoPoSplat for evaluation to ensure complete fairness.

More Details of SPFSplat Results. According to the official training configuration provided for SPFSplat, 200,000 training iterations are required. We use the official 2-view checkpoint from the repository and further fine-tune them for 200,000 iterations on the multi-view setting to ensure sufficient training of SPFSplat.

More Details of VicsSplat Results. For VicaSplat, the official code specifies the training requirements for each step on RE10K, and we strictly follow the training and fine-tuning procedures provided by the official code. For training on ScanNet, we follow our training and fine-tuning settings, and, as specified by the official guidelines, we perform point distillation before training.

More Details of AnySplat Results. Since the training

dataset of AnySplat is approximately four times larger than the number of scenes in our RE10K training set and 95 times larger than the number of images in ScanNet. Therefore, we report both the zero-shot results of the generic model provided by AnySplat (denoted as AnySplat), as well as the results obtained by training on RE10K and ScanNet following the official instructions (denoted as AnySplat*). Since AnySplat itself is trained on images with a resolution of 448, using different input resolutions leads to severe artifacts. Therefore, we use 448-resolution inputs for zero-shot testing with AnySplat. It is worth noting that the input image content is kept exactly the same as in other models, with only the resolution being different. For novel view synthesis tests, we render the 3DGS outputs of the models at a resolution of 256×256, ensuring that all models are evaluated at the same resolution. (Rendering at 448 resolution and then resampling to 256 yields even worse results.) Moreover, since AnySplat uses VGGT as its backbone and only supports inputs at 14× resolution, we train AnySplat* at a resolution of 266×266, and adopt a testing strategy similar to that of AnySplat.

Results show that while the visual quality of AnySplat is acceptable, its reconstructed scenes exhibit some distortions and deformations. This distortion is not easily noticeable when viewing AnySplat results in isolation, but becomes much more apparent when test views are aligned with ground-truth views for evaluation (following the protocol in NoPoSplat). In many scenes, such distortions are clearly observed after this alignment. Even after fine-tuning on the corresponding scenes, achieving improvements and reaching the performance reported by the official implementation, there remains a significant gap compared to our method.

A2. More Implementation Details of Modulation in Asymmetric Dual-Flow Decoder

Inspired by the Adaptive Layer Normalization in DiT, we adopt a similar modulation strategy. Specifically, an MLP predicts three modulation parameters, *i.e.* *scale*, *shift*, and *gate*, from the camera token at each step. Since the camera tokens are continuously updated within the decoder blocks, after self-attention layer, a separate MLP predicts a new set of modulation parameters from the updated camera token. The normalization parameters (scale and shift) and an additional scaling parameter (gate) are applied as follows: before attention, we perform $\hat{t}_i^{\mathbf{I}} \leftarrow \hat{t}_i^{\mathbf{I}} \times (1 + \text{scale}) + \text{shift}$; after attention, we update as $\hat{t}_i^{\mathbf{I}} \leftarrow (1 + \text{gate}) \times \hat{t}_i^{\mathbf{I}}$.

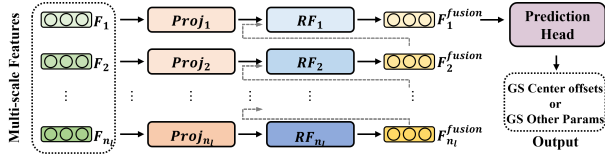


Figure A1. Structure of our Gaussian Prediction Head.

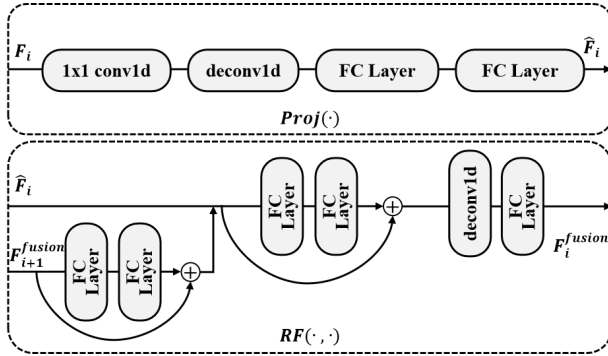


Figure A2. Network details in our Gaussian Prediction Head.

A3. More Implementation Details of Gaussian Prediction Heads

In this section, we further elaborate on the detailed design of our Gaussian Prediction heads, as illustrated in Fig. A1. our Gaussian Prediction heads take the multi-scale features from the fused token decoder outputs as input. In our implementation, we follow the DPT head by selecting features from the 0-th, 6-th, 9-th, and 12-th layers of the decoder as inputs F_1, F_2, F_3, F_4 to the Gaussian Prediction head.

The multi-scale features are first individually processed by a projection module, denoted as $Proj(\cdot)$, as illustrated in the upper part of Fig. A2. This module consists of a 1×1 Conv1D layer for channel transformation, followed by a deconvolution layer for upsampling. Subsequently, two fully connected layers are used for linear mapping to get \hat{F}_i . Ultimately, all features are unified to the same number of channels, which is set to 256 in our implementation.

Subsequently, we perform deep-to-shallow fusion from feature \hat{F}_4 to feature \hat{F}_1 , as shown in the lower part of Fig. A2. For feature \hat{F}_4 , we directly apply a residual module composed of two fully connected layers for further feature transformation. For shallower features \hat{F}_i , we first add the fused feature from the deeper layer F_{i+1}^{fusion} after passing it through a residual module consisting of two fully connected layers, and then apply another residual module with two fully connected layers for feature transformation. Finally, the output is upsampled using a deconvolution module and further processed by a fully connected layer to obtain F_i^{fusion} .

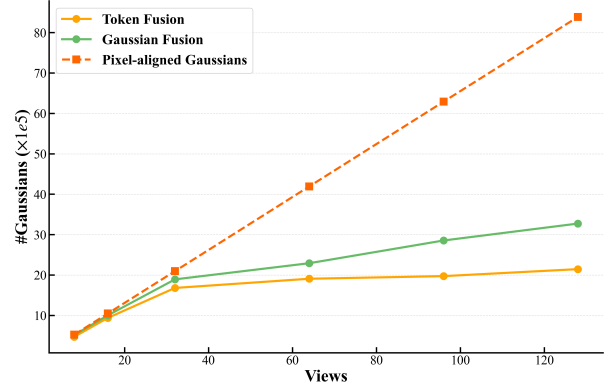


Figure A3. Number of Gaussians with increasing input views for pixel-aligned GS, Gaussian fusion methods, and our Token Fusion operation.

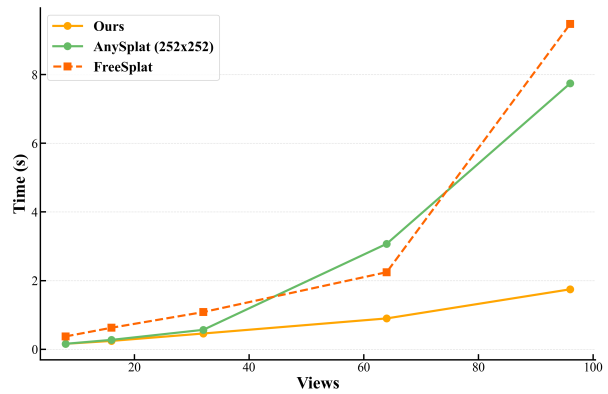


Figure A4. Inference time with increasing number of input views.

A4. More Implementation Details of Pose Heads

The pose head takes the camera token output from the Asymmetric Dual-Flow Decoder as input and consists of activation functions and fully connected layer. Specifically, we use a ReLU activation function and a fully connected layer with dimensions (768, 7) in this work. The pose head outputs camera rotation (as a quaternion) and translation, which are then converted to unit dual quaternions for loss computation. Our pose head is designed with a simple structure, as the Asymmetric Dual-Flow Decoder effectively disentangles camera features, allowing accurate predictions with minimal complexity.

A5. More Experimental Analysis

A5.1. Efficiency

We investigate the impact of different fusion methods on the number of Gaussian primitives and show the result in



Figure A5. Visualization Results with increasing number of input views.

Fig. A3. As the number of input views increases, the number of pixel-aligned Gaussian primitives grows linearly. In contrast, using Gaussian fusion modules in 3D space directly or our Token Fusion operation helps stabilize the growth of Gaussians. It can be observed that as the number of views increases, our Token Fusion operation leads to a much slower growth in the number of Gaussians, making the count more stable compared to Gaussian fusion. We investigate how the model’s inference time changes as the number of input views increases and show the result in Fig. A4. As other models experience excessive growth in model size and memory usage with increasing views, we mainly compare with FreeSplat and AnySplat. Since AnySplat only supports up to $14\times$ resolution, we use a resolution of 252×252 , while FreeSplat and ours use 256×256 . Our method maintains more stable inference time as the number of views increases. This is because, unlike Gaussian fusion methods where computation in the Gaussian prediction stage remains proportional to the number of input images, our approach performs fusion first, fully decoupling the number of Gaussians from the number of images, resulting in more stable inference time.

A5.2. Visualization Results with Increasing Number of Views

We further demonstrate the impact of increasing the number of input views on novel view synthesis. Starting with the first and last views, we gradually add more intermediate views. As shown in Fig. A5, additional input views progressively enhance scene completeness and visual details, especially in challenging regions such as railings.

A6. More Visualization Results

We present additional qualitative comparisons with baselines on the RE10K and ScanNet datasets in Fig. A6 to Fig. A10, further demonstrating the effectiveness and improvements of our method. Our approach achieves stable and superior performance across varying numbers of input images and diverse input data.

A7. Video Demo

The project webpage includes comparison videos between our approach and state-of-the-art methods. Whether in rendered videos or when observing the entire scene from a distance, our method consistently exhibits more complete and coherent structures, whereas existing methods suffer from blurring or defocus-like artifacts, and some even exhibit severe structural issues. For example, when running SPFSplat and VicaSplat with more input views than used during training, we observe significant scene compression at the boundaries, making it difficult to effectively extend outward. FreeSplat projects Gaussians into 3D space using depth maps, resulting in a large number of floating artifacts. In the left-side close-up rendering video of AnySplat, noticeable cracks caused by unsuccessful Gaussian fusion can be observed near the mirror at the beginning, and multiple issues arising from 3D Gaussian fusion are also clearly visible in the long-range scene. Furthermore, our method exhibits remarkable generalization ability, as evidenced by the reconstruction results on scenes from different datasets and **in-the-wild data casually captured with mobile phones.**

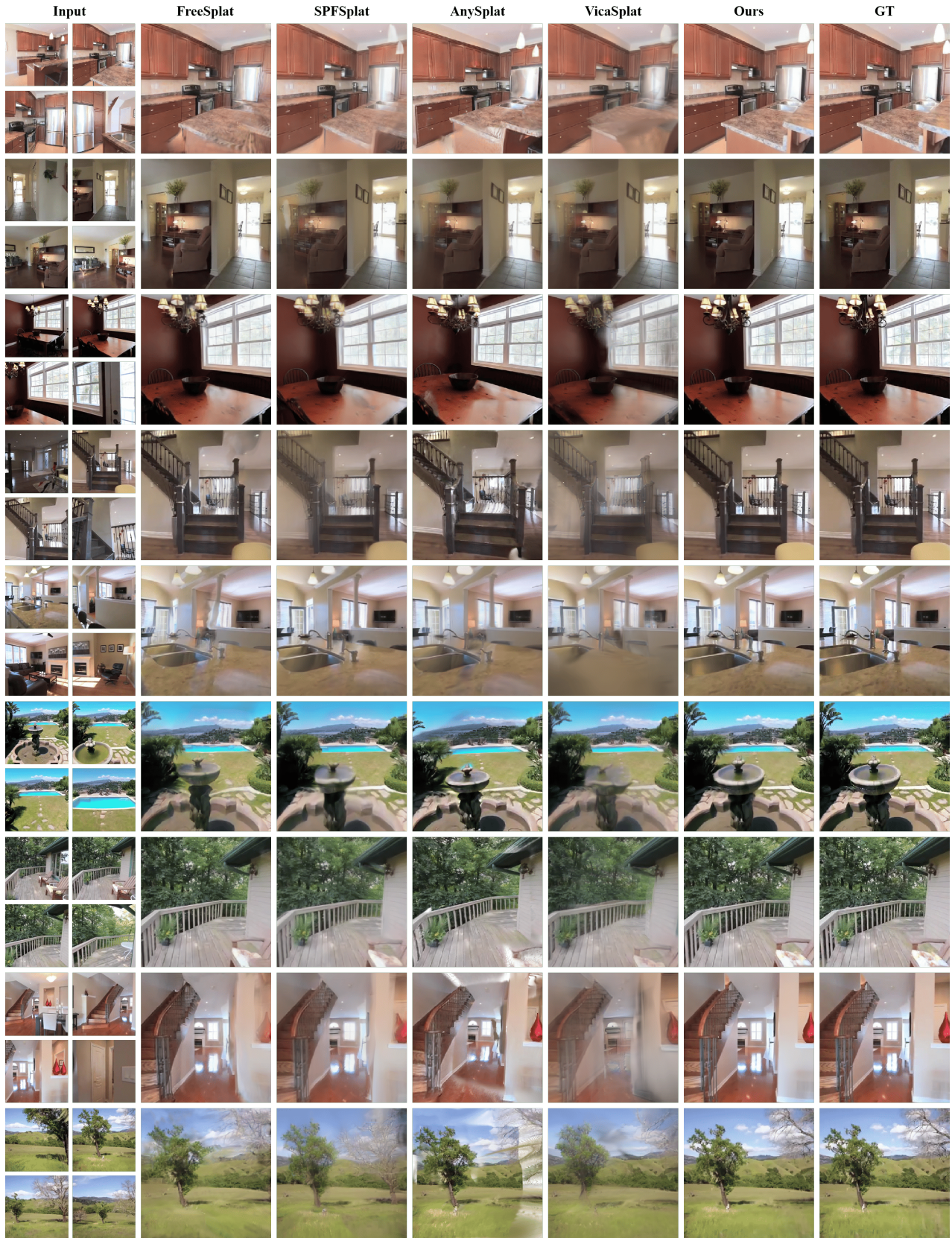


Figure A6. More qualitative comparisons on RE10K with 4 input images.

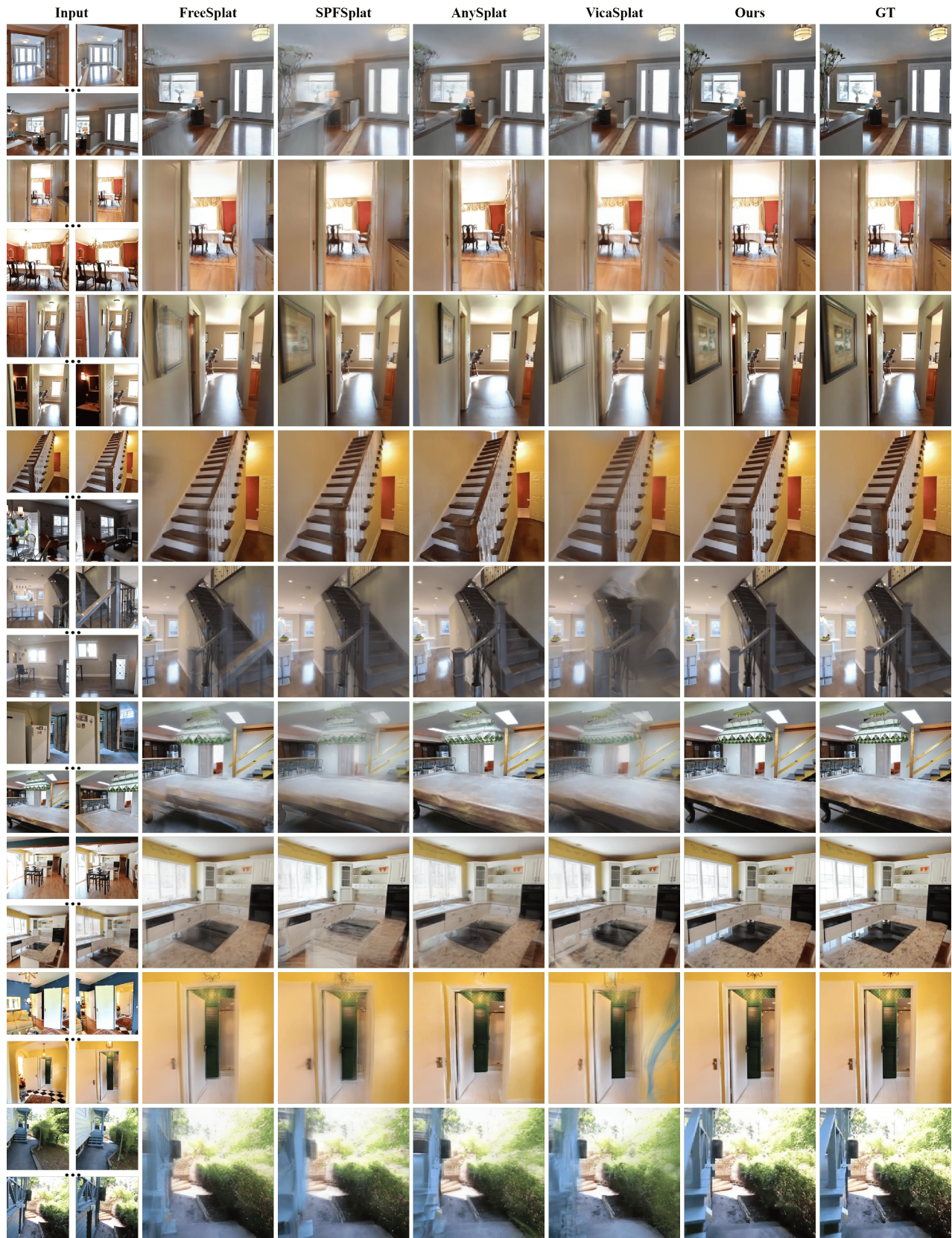


Figure A7. More qualitative comparisons on RE10K with 8 input images.

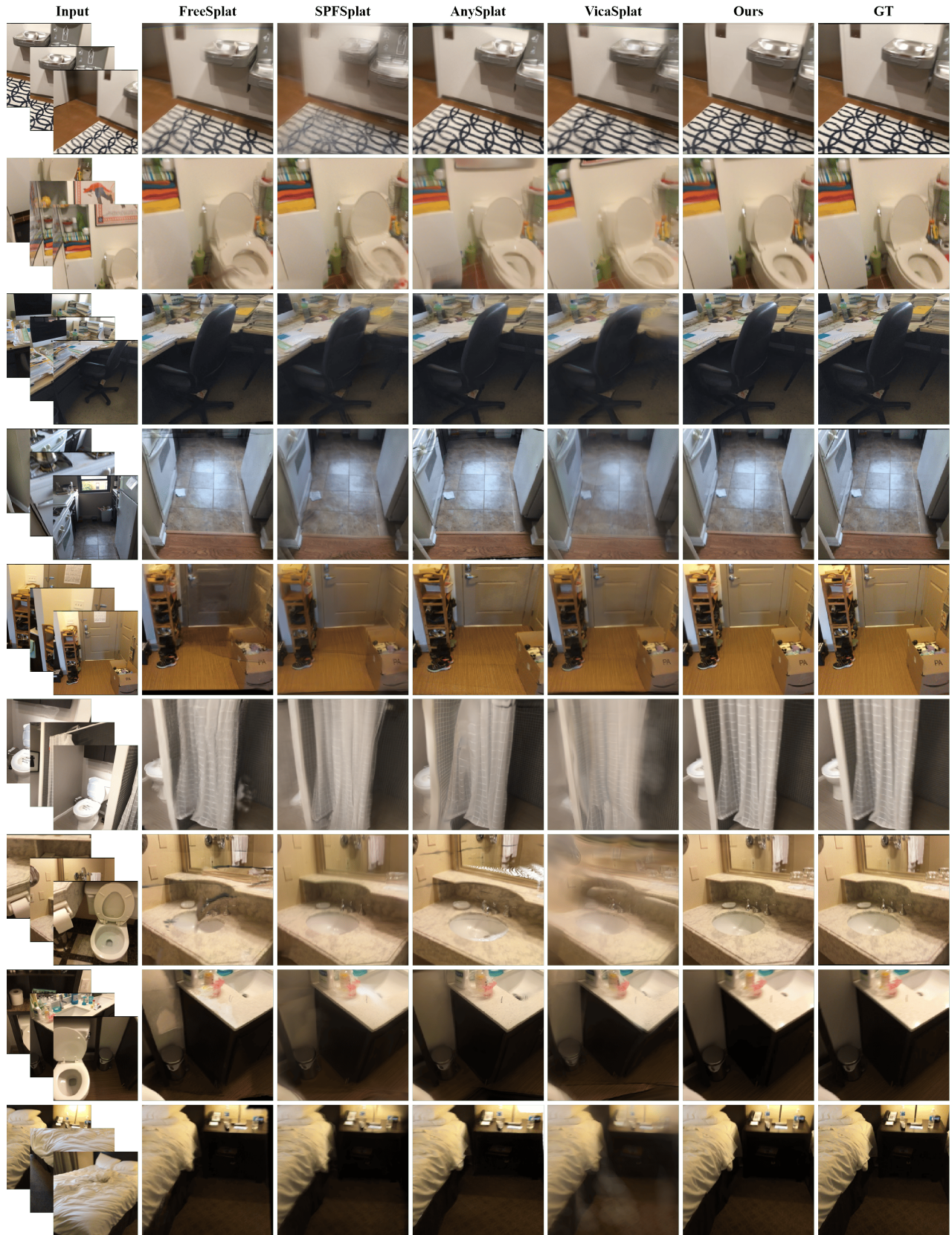


Figure A8. More qualitative comparisons on ScanNet with 3 input images.

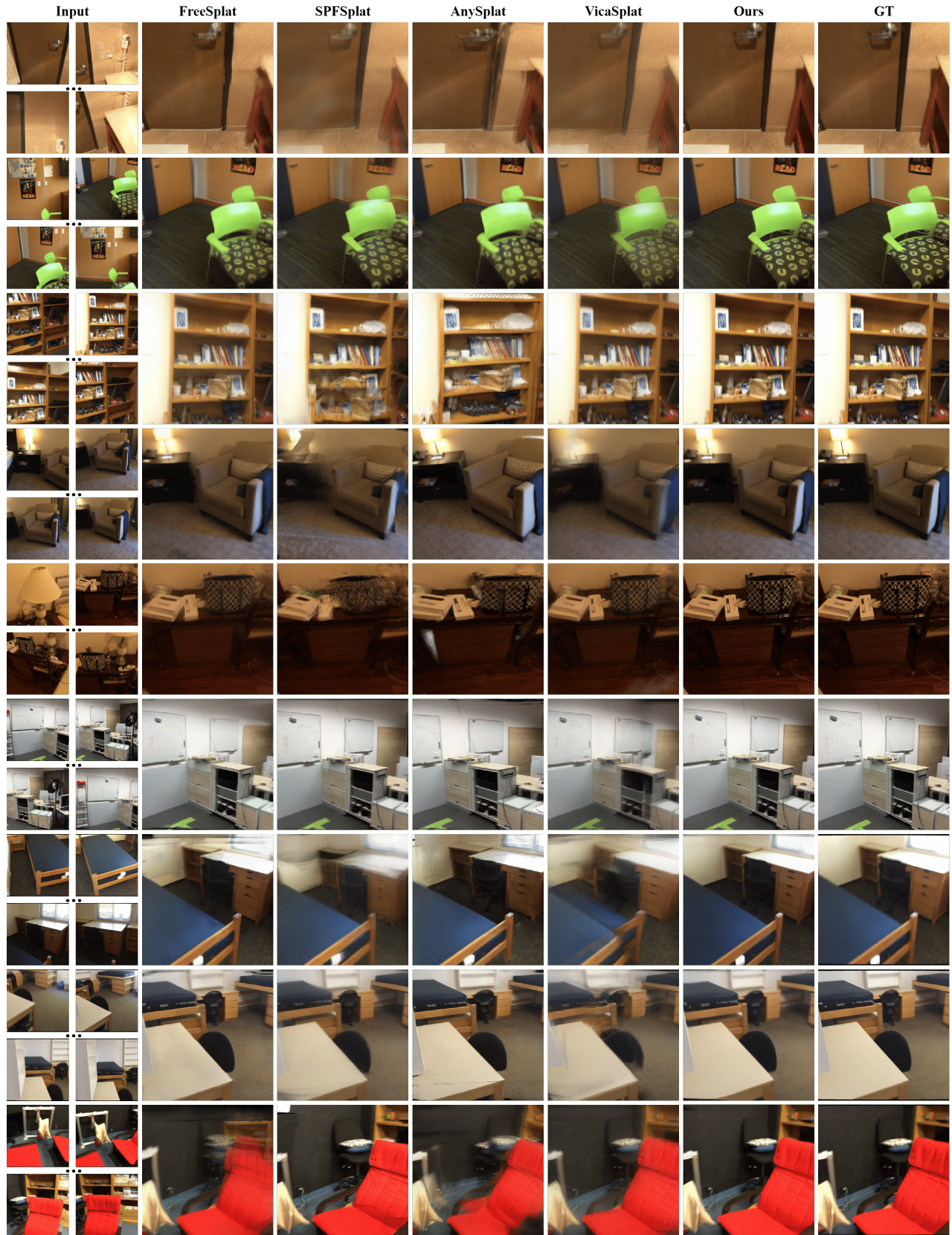


Figure A9. More qualitative comparisons on ScanNet with 10 input images.

